Journal Name

Machine learning-aided quantification of 3D angiogenic vasculature in multiculture microfluidic platform[†]

Wonjun Lee,[a‡] Byoungkwon Yoon,[b‡] Jungseub Lee,[a] Sangmin Jung,[a] and Noo Li Jeon[*acd]

A plethora of in vitro models have been the focus of intense research to truly mimic the native physiological system. Among them, organ-on-a-chip or microfluidic devices gave notable results in reconstructing reproducible three-dimensional vascularized organ-specific microenvironments using various approaches. However, because of the absence of effective quantification methodologies for assessing the phenotypic variation of on-chip microvascular networks, these benefits have not yet translated to "bench-to-bedside" deployment of microfluidic platforms. To this end, we introduce a novel machine learning-assisted 3D analysis pipeline that is capable of extracting major assessment parameters quantifying on-chip MVNs' phenotypic variation. Meso-skeletal depiction of the microvasculature and skeleton segmentation via improved graph convolutional network allowed for a more accurate structural analysis of the angiogenic network than any other approach. We show that our method outperforms conventional projection base analysis by giving satisfactory concordance with the manual investigation. Our experiment indicates that our method can offer a chance to elucidate the essence of vessel physiology that otherwise would have been overlooked and help establish reliable preclinical models for biopharmaceutical applications.

1 Introduction

Microvascular networks (MVNs), working as a mediator between localized tissues and the circulatory system, is universally credited for their pivotal role in different pathophysiological scenarios. Ranging from oncology[1] to tissue regeneration[2,3], MVNs actively engage and interact with the microenvironment and regulate various physiological phenomena. Recognizing its significance, several studies have been conducted to establish a platform that can reconstitute complicated functions of the microvascular environment in the human body. Along with in vivo platforms, in vitro reconstruction of vascular tissues has advanced rapidly in recent decades. And the advent of a microfluidic or organ-on-a-chip platform enabled unprecedented sophistication of emulation by allowing 3D co-culture of endothelial cells (ECs) and associated stromal cells[4–6]. Therefore, paving the way for a human-centric

[a] Department of Mechanical and Aerospace Engineering, Seoul National University, Seoul 08826, Republic of Korea. E-mail: njeon@snu.ac.kr
[b] Department of Mechanical Engineering, Korea University, Seoul 02841, Republic of Korea
[c] Institute of Advanced Machines and Design, Seoul National University, Seoul 08826, Republic of Korea
[d] Institute of Bioengineering, Seoul National University, Seoul, 08826, Republic of Korea
† Electronic Supplementary Information (ESI) available: [details of any supplementary information available should be included here]. See DOI: 00.0000/00000000.
‡These authors contributed equally to this work.

preclinical screening system, it has been the subject of intense research.

Nevertheless, these advantages have not yet translated to "bench-to-bedside" deployment of microfluidic platforms due to the lack of effective quantification techniques for evaluating the phenotypic variation of MVNs in 3D. Some exclusive features of microfluidic system distinguish it from MVN investigation in other in vivo or 2D in vitro platforms: 1) random lumenization and root of angiogenesis trigger severe heterogeneity to overall network architecture, 2) fuzzy, non-uniform staining may result in highly noisy data with excessive speckles. Existing analytical approaches are rendered ineffective as a result of these difficulties. Their methods are primarily appropriate for generic vasculogenesis analysis, which is insufficient for on-chip angiogenesis and frequently necessitates the use of additional complex apparatus for the elaborate reconstruction of 3D MVNs, putting them out of reach of some researchers[7–10]. Work-around adopted by academia was to analyze MVNs on the basis of 2D-slices or maximum intensity projection (MIP) images. However, considering the 3D nature of vasculature, it is obvious that this strategy would lead to erroneous results with a significant loss in meaningful data[11].

To this end, in this study, we propose a novel 3D analysis pipeline well suited for on-chip angiogenesis evaluation. The MicroVascular Injection-Molded Plastic Array 3D Culture (MV-IMPACT) platform, designed as an injection molded mass-
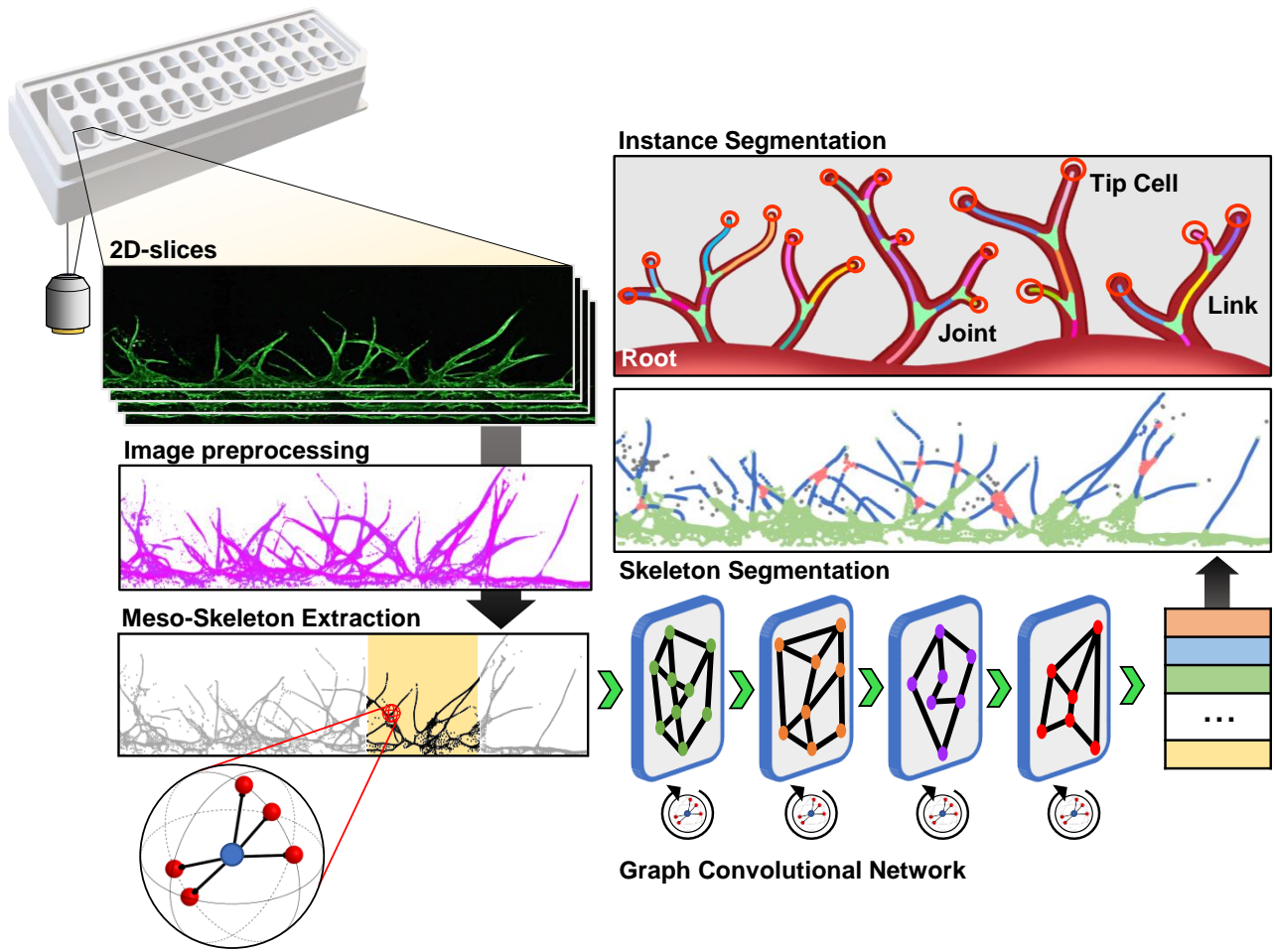
Fig. 1 Representation of the work flow performed by proposed pipeline. Overall analysis is mostly automated to minimize individual bias and alleviate user fatigue.

producible polystyrene (PS) device in a standardized 96-well plate SBS format, was used to collect various angiogenesis data. Utilization of geometrically modeled spontaneous capillary flow allowed for reliable and repeatable liquid patterning, which helped to produce uniform and high-quality data for a data-driven approach.

After converting the obtained confocal captured data into point cloud format, the 3D analysis of MVNs was carried out. Pipeline's workflow consists of image preprocessing, meso-skeleton extraction, skeleton segmentation, and instance segmentation (Fig. 1). Meso-skeleton composed of skeletal curves and sheets, gave an elaborate summary of the original vascular network into skeleton data while preserving the network's major topological property. Next, an improved graph convolutional network (GCN) algorithm was implemented to segment the skeleton based on local geometric structure and neighborhood connectivity. Predicted segments were partitioned at the instance level and used to obtain final evaluation metrics. As a proof of concept, we show our method's superiority over the conventional MIP approach by comparing the resultant parameter values of the lung fibroblasts (LFs) induced angiogenesis dataset. Overall, our methodology is of generic impact and easily transposable to more advanced microfluidic sys-

tems or other vasculature analysis tasks. We envision that our pipeline will aid future research on vascularized microphysiological systems.

2 Materials and methods

2.1 Fabrication of MV-IMPACT

Polystyrene (PS) injection molding was performed at R&D Factory (Korea). The aluminum alloy mold core was processed by machining and polishing. The clamping force at the time of injection was set to 130 ton with a maximum injection pressure of 55 bar, 15 s of cycle time, and a 220 °C nozzle temperature. Biocompatible and transparent substrate was bonded to injection-molded PS body to complete the device.

2.2 Cell preparation

Human umbilical endothelial cells (HUVECs; Lonza, Switzerland) were cultured in endothelial growth medium 2 (EGM-2; Lonza) and used in experiments between passage 4-5. Lung fibroblasts (LFs; Lonza) were cultured in fibroblast growth medium 2 (FGM-2; Lonza) and passages 7 was used for experiments. Cells were incubated at 37°C and 5% CO_2 and grown to 70-80% confluency
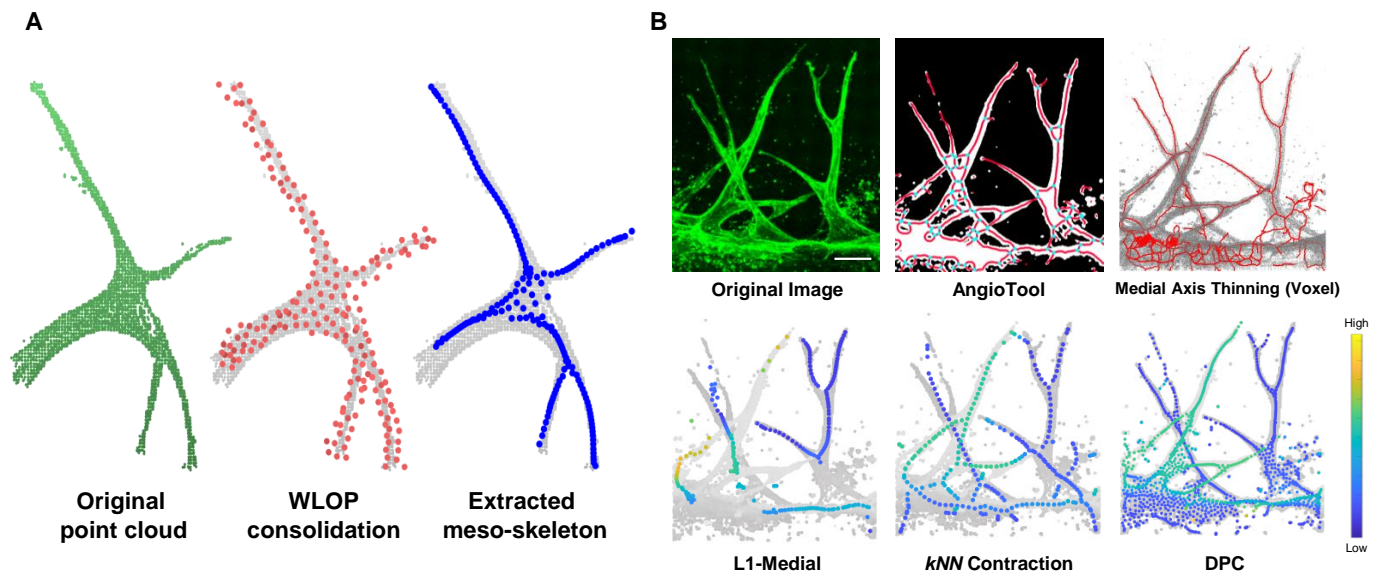
Fig. 2 Overview of our utilized meso-skeleton extraction. (A) Meso-skeleton extraction process of deep point consolidation. Given the input point cloud, its surface representation is further consolidated with WLOP consolidation. Through joint optimization, meso-skeleton representing overall network architecture is formed. (B) Qualitative comparison with the competitive skeletonization methods, i.e., AngioTool [12], medial axis thinning of voxels [13,14], L_1-medial skeleton [15], kNN contraction skeleton [16], and deep point consolidation (DPC) [17]. The color changed from light to dark represents the height along the z-axis from high to low. Artifacts triggered by the root of angiogenesis and clusters of cell debris cause skeletal data to fail to provide critical morphological features about the given angiogenic network. Scale bars, 100. μm.

before chip loading. Cultured cells were dissociated using 0.25% trypsin–EDTA (HyClone, USA). Afterward, harvested cells were resuspended in bovine fibrinogen solutions and the concentrations were properly adjusted according to the experimental requirements.

2.3 Hydrogel and cell patterning

Prior to loading, the surface of injection-molded PS chips was hydrophilzed with plasma surface treatment at 70W for 3 min (Femto Science, Korea). The following steps were taken to pattern the cells in the chip: central channel was patterned with 1 μL of acellular bovine fibrinogen solution (final concentration 2.5 mg mL^{-1}; Sigma, USA) mixed with bovine thrombin (0.5 UmL^{-1}, Sigma). After waiting 5 min for the gels to polymerize, LFs (final concentration 6×10^6 mL^{-1}) encapsulated fibrinogen, thrombin mixture was patterned into the upper side channel and similarly left to clot at room temperature for 5 min. HUVECs suspension (final concentration 1×10^6 mL^{-1}) was then introduced to the contralateral channel. Patterned chips were tilted by 90 degrees and incubated for 30 min so that HUVECs can fully adhere to fibrin gel surface. After that, EGM-2 was added to the reservoirs, and the chips were kept in an incubator. To not disturb the gradient of paracrine factors, cell culture media was replenished once after 2-3 days of co-culture. During this process, a fresh medium was injected only into the upper reservoir for generation of shear stress and interstitial flow [18].

2.4 Immunostaining and data preprocessing

Tissues in the device were fixed using 4% (w/v) paraformaldehyde (Biosesang, Korea) in phosphate-buffered saline (Gibco) for 15 min, followed by permeabilization with a 20 min immersion in 0.15% Triton X-100 (Sigma). The samples were then blocked with 3% bovine serum albumin (Sigma) for 1 h. Endothelial cell (EC)-specific staining was done with 488 fluorescein-labeled Ulex Europaeus Agglutinin I (Vector, UK), which was prepared at a 1:1000 ratio of dye in BSA for 12 h at 4°C. The whole aforementioned process was conducted through media reservoirs of the chip without disassembly.

2D slices of angiogenic networks were acquired every 2.175 μm using confocal microscopy (Nikon Ti2, Japan). Obtained images were later stacked in the z-axis to reconstruct 3D voxelized vascular networks. Afterward, the 3D matrix was binarized via median-thresholding and then converted to point cloud data based on voxel size. Mean filter was used to remove the outliers among this procedure.

2.5 Meso-skeleton extraction

To comprehensively describe angiogenic networks without any loss of significant data, we adopt *Wu et al.*'s method to extract meso-skeleton from the original point cloud data (Fig. 2A) [17]. Details of this skeleton extraction algorithm will be omitted for brevity.

2.6 Skeleton segmentation

Extracted skeleton is segmented using graph convolutional network. Here taking *Dynamic Graph CNN* [19] (DGCNN) as a back-

bone, we replace maxpooling operation with attention module. Let $\mathscr{P} = \left\{ \mathbf{x}_i \in \mathbb{R}^C \right\}_{i=1}^N$ be a C dimensional point set with N points. To capture each point's local geometric structure, we construct a directed graph $\mathscr{G} = (\mathscr{V}, \mathscr{E})$ composed of a finite set of vertices $\mathscr{V}$ and edges $\mathscr{E} \subseteq \mathscr{V} \times \mathscr{V}$ using k-nearest-neighbors (k-NN). Specifically, for a target point $\mathbf{x}_i$, its neighborhood set is constructed as $\mathscr{N}(\mathbf{x}_i) = \{\mathbf{x} \in \mathscr{P} : \|\mathbf{x} - \mathbf{x}_i\|_2 < \|\mathbf{x}_i - \mathbf{x}_k\|_2\}$, where $\mathbf{x}_k$ is the k-th nearest point from $\mathbf{x}_i$. Graph's edge feature is then simply computed in form of $\mathbf{x}_j - \mathbf{x}_i$, where $\mathbf{x}_j \in \mathscr{N}(\mathbf{x}_i)$. Afterward, nonlinear function $h_\Theta : \mathbb{R}^C \times \mathbb{R}^C \to \mathbb{R}^{C'}$ is applied to individual points, coupled with edge features, to map feature vectors onto a higher dimensional space:

$$\mathbf{x}_i' = h_\Theta \left(\mathbf{x}_j - \mathbf{x}_i, \mathbf{x}_i \right) \in \mathbb{R}^{k \times C_{out}}, \quad \mathbf{x}_j \in \mathscr{N}(\mathbf{x}_i) \qquad (1)$$

Multilayer perceptron (MLP), consisting of 2D 1×1 convolutional layer followed by a batch normalization layer[20] and a leaky-ReLU activation function[21], is adopted here as a nonlinear function. Outputted features from MLP are then fed into our attention modules to aggregate features of k-NN.

Attentive pooling. Since max-pooling only focus on prominent configurations while discarding details, attention pooling is instead used to aggregate neighbor's features[22]. Attentional weights of each channel is measured by the *Squeeze-and-Excitation* block, so that the module can dynamically adapt to the local distribution of the neighborhoods[23,24]. Here, we simply denote our block as M_α.

$$\alpha_i = M_\alpha \left(\mathbf{x}_i' \right) \in \mathbb{R}^{k \times C_{out}}, \quad \mathbf{x}_j \in \mathscr{N}(\mathbf{x}_i) \qquad (2)$$

To retain sensitivity to salient feature and prevent information oversaturation, attentional weights are normalized across all the neighbors of a query point $\mathbf{x}_i$. Therefore, the final output of the proposed module can be formulated as follows:

$$\mathbf{x}_i^{att} = \sum_{j \in [1,k]} \frac{exp(\alpha_{i,j})}{\sum_{l \in [1,k]} exp(\alpha_{i,l})} * \mathbf{x}_i' \in \mathbb{R}^{C_{out}} \qquad (3)$$

where $*$ represents the element-wise matrix multiplication (Hadamard product).

Spherical feature aggregation. We observe that graph generated by skeleton data is highly homophilious. Therefore, feature uniformity with respect to the point's spatial neighbors should be guaranteed. To this end, we predict the weights $\mathbf{w}_i$ of the spatial neighbors and aggregate spatial neighbors' feature in a weighted manner. Neighboring points are transformed from Cartesian to spherical coordinates where query point is the origin. But without kernel discretization, spherical coordinate values are directly utilized with deviations to learn local geometric information. Afterward. attentional weights for each neighboring point are measured by MLP. However, instead of 2D convolutional layer, 1D convolutional layer, which is shared even within every point, is adopted to compute the attentional weights. In brief, weights can be calculated as:

$$\mathbf{w}_i = M_\mathbf{w} \left(\mathbf{r}_i, \theta_i, \phi_i, \mathbf{r}_i - \bar{r}_i, \theta_i - \bar{\theta}_i, \phi_i - \bar{\phi}_i \right) \in \mathbb{R}^k \qquad (4)$$

where $\mathbf{r}_i, \theta_i, \phi_i$ are radius, polar angle, and azimuth angle com-

ponents of $\mathbf{x}_i$'s neighboring points and $M_\mathbf{w}$ is the applied MLP. Output weights can be casted into $N \times k \times C_{out}$ matrix by tiling along the channel dimension. After weight normalization, we aggregate features of spatially nearest neighbor points into features of a single point $\mathbf{x}_i$. Therefore, given the set of spatial neighbors' features $\mathbf{f}_i = \left\{ \mathbf{f}_i^1, \mathbf{f}_i^2 \cdots \mathbf{f}_i^k \right\} \in \mathbb{R}^{k \times C_{out}}$ from $\mathbf{x}^{att}$, the final output of the proposed module can be formulated as follows:

$$\mathbf{x}_i^{final} = \mathbf{x}_i^{att} + \sum_{j \in [1,k]} \frac{exp(\mathbf{w}_{i,j})}{\sum_{l \in [1,k]} exp(\mathbf{w}_{i,l})} * \mathbf{f}_i^j \in \mathbb{R}^{C_{out}} \qquad (5)$$

Network architecture. Constructed network's configuration is summarized in Fig. 4A. After spatial transformation, input data goes through three consecutive modified EdgeConv layers. Each modified EdgeConv layer is composed of two shared fully-connected layers (64,64) followed by the previously described modules. Graph is dynamically updated during this process and a newly generated graph is passed on to the next layer. Information from each modified EdgeConv layer is aggregated with a shared fully-connected layer (1024). This multi-scale feature is then concatenated with the outputs of previous layers using skip-connections. Finally, pointwise features are transformed by three shared fully-connected layers (256, 256, 128), and per-category segmentation scores are computed. Through this network, the input skeleton is segmented into five different parts: i.e., root, joint, link, noise, and tip-cell.

Model training. LF-induced angiogenesis dataset from the MV-IMPACT platform was used for training. This dataset contains 400 skeleton point clouds. Each point belongs to one of 5 categories—e.g. root, joint, link, noise, and tip cell. The ground truth has been manually annotated and cross-checked by the authors of this study. For model evaluation, we performed 5-fold cross validation with microaveraging. Our network was trained on a single Nvidia RTX 3070 Ti GPU with stochastic gradient descent (SGD) optimizer. We applied common augmentations on-the-fly in the training session, including random azimuth rotation (up to 15° degrees), random flipping, shuffling, and random Gaussian noise perturbation. To handle severe class imbalance, the cross-entropy loss was balanced with empirically optimized weight terms:

$$\mathscr{L}(\theta) = -\frac{1}{N} \sum_{i=1}^N \sum_{j=1}^\Gamma \Omega_j \mathbf{y}_{ij} \log \mathbf{p}_{ij} \qquad (6)$$

2.7 Instance segmentation

The segmented skeleton is further clustered to construct a 3D graph that encompasses the morphological information of the angiogenic network. Since individual joints and links are in the shape of regional clusters, *Density-Based Spatial Clustering of Applications with Noise* (DBSCAN)[25] is used for individualization. After clustering, DBSCAN is once more utilized to determine the connectivity between links and joints.

2.8 Pipeline evaluation

LF-induced angiogenesis dataset precluded from model training was used for pipeline assessment. We first utilize our pipeline

to extract commonly used MVN assessment parameters, which are total vessel length, average vessel length, number of bifurcations, number of angiogenic sprouts, average sprouting length, average vessel tortuosity, and average branching depth of angiogenic sprouts[26–30]. We then compare our results with the analysis results of the conventional MIP method. Here, we choose AngioTool[12] as a baseline by virtue of its prevalence and versatility. In the case of evaluation metrics that are not supported by vanilla Angiotool, values were derived through further computation based on the skeleton taken from Angiotool. Detailed information about the modified version is provided in Supplementary Material (Fig. S1†).

The accuracy of the vessel structural metrics was tested using absolute error, which is defined as the closeness of a measured value to a ground-truth. And measurements having a small absolute error were regarded as being accurate. Defined absolute error is formulated as follows:

$$A_{i,j} = \left| Y_{i,j} - G_{i,j} \right| \tag{7}$$

where $Y_{i,j}$, and $G_{i,j}$ represents measured vessel structure metric of ith image from j^{th} method and the corresponding ground-truth value obtained by manual analysis, respectively. In addition, following the variable transform from the Brown-Forsythe test of variance, precision of each method was also taken into account for evaluation which is formulated as follows:

$$P_{i,j} = \left| E_{i,j} - \widetilde{E}_j \right| \tag{8}$$

where $\widetilde{E}_j$ is the median of $E_{i,j}$ across images[31,32].

2.9 Statistical analysis

Using Prism (GraphPad, USA), statistical comparisons of the values were obtained from an paired two-tailed Student's t-test analysis, with the threshold for statistical significance set at *p < 0.05. **p < 0.005; ***p < 0.0005; and ns (not significant). The standard error of the mean (SEM) is presented in error bars.

3 Results and discussion

3.1 Microfluidic model for angiogenesis data acquisition

MV-IMPACT is made up of a single PS body that houses the media reservoir and microfluidic patterning geometries, attached with polycarbonate (PC) film substrate (Fig. 3). The designed well consists of 3 microchannels that are disposed in parallel and partitioned by channel height. Working as a pathway of nutrition and oxygen, the upper channel (UC) and lower channel (LC) are directly exposed to the media chamber for cell feeding. With a row pitch of 9mm and a column pitch of 4.5mm, the well interval fully complies with that of commercial 384-well plates. As a result of its standardized form factor compatibility, MV-IMPACT is entirely adaptable with the vast majority of laboratory equipment, ranging from microscopes to automated fluid dispensers.

The patterning principle for MV-IMPACT lies in spontaneous capillary flow patterning (SCP) of droplets facilitated by air plasma-induced hydrophilic surface modification[30]. Fluid movement independent of external energy stabilizes and ensures re-
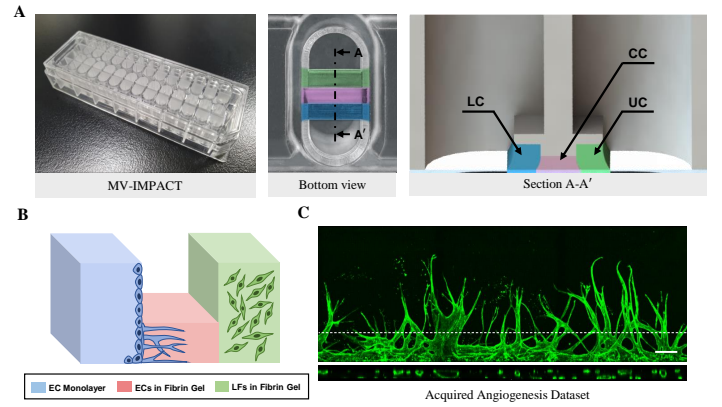

Fig. 3 Angiogenesis data acquisition using HUVECs and LFs. (A) Photograph and conceptual image of MV-IMPACT chip. Through a standardized 384-well plate format, high-throughput and efficient assay of angiogenesis were possible. (B) Configuration of the microfluidic device for modeling angiogenesis into 3D ECM. (C) Representative confocal image of the acquired dataset with a cross sectional view at white dashed line showing 3D lumen structure of vasculature. Scale bars, 500 μm.

producibility of experimental procedures. recent years, initiatives to incorporate deep-learning into numerous disciplines have been made, with varying degrees of success, particularly in biomedical applications. This triumph was largely made possible by the collection of enough data[33]. Data-driven approach have enabled models to learn salient aspects without miscellaneous handcrafted features, enabling different tasks that were before thought to be impossible[34]. In light of this, our device offers the possibility for technical advancements that conventional soft lithographic polydimethylsiloxane (PDMS) devices can not provide. Our platform's mass-productive, user-friendly, and dependable properties will ease the data generation process and assure its quality, facilitating the subsequent learning step.

3.2 Meso-skeleton depiction of angiogenic network

The majority of vessel evaluation techniques use a completely shrunk skeleton to depict MVNs in graph form[9,10,35]. The points of the skeleton are categorized as branch or non-branch based on the directionality degree of the local context in the case of point clouds or neighborhood connectivity in the case of voxels, and are then utilized for structural analysis. However, this type of binary representation typically fails to encompass key topological information about the angiogenic network (Fig. 2B). In particular, the root of angiogenesis and clusters of cell debris trigger severe shape distortion of the extracted skeleton. These issues are difficult to regulate or fix, complicating the analysis and contributing to inconsistent outcomes.

To overcome these issues, we represent MVNs in the form of meso-skeleton for analysis, which is close to the raw contraction form of input data, rather than a fully shrunk skeleton. Because initial raw contractions are unlikely to properly summarize the original structure, most point cloud skeletonization algorithms use their own methods to confirm branchpoint and implement corresponding additional contractions to confirm the form
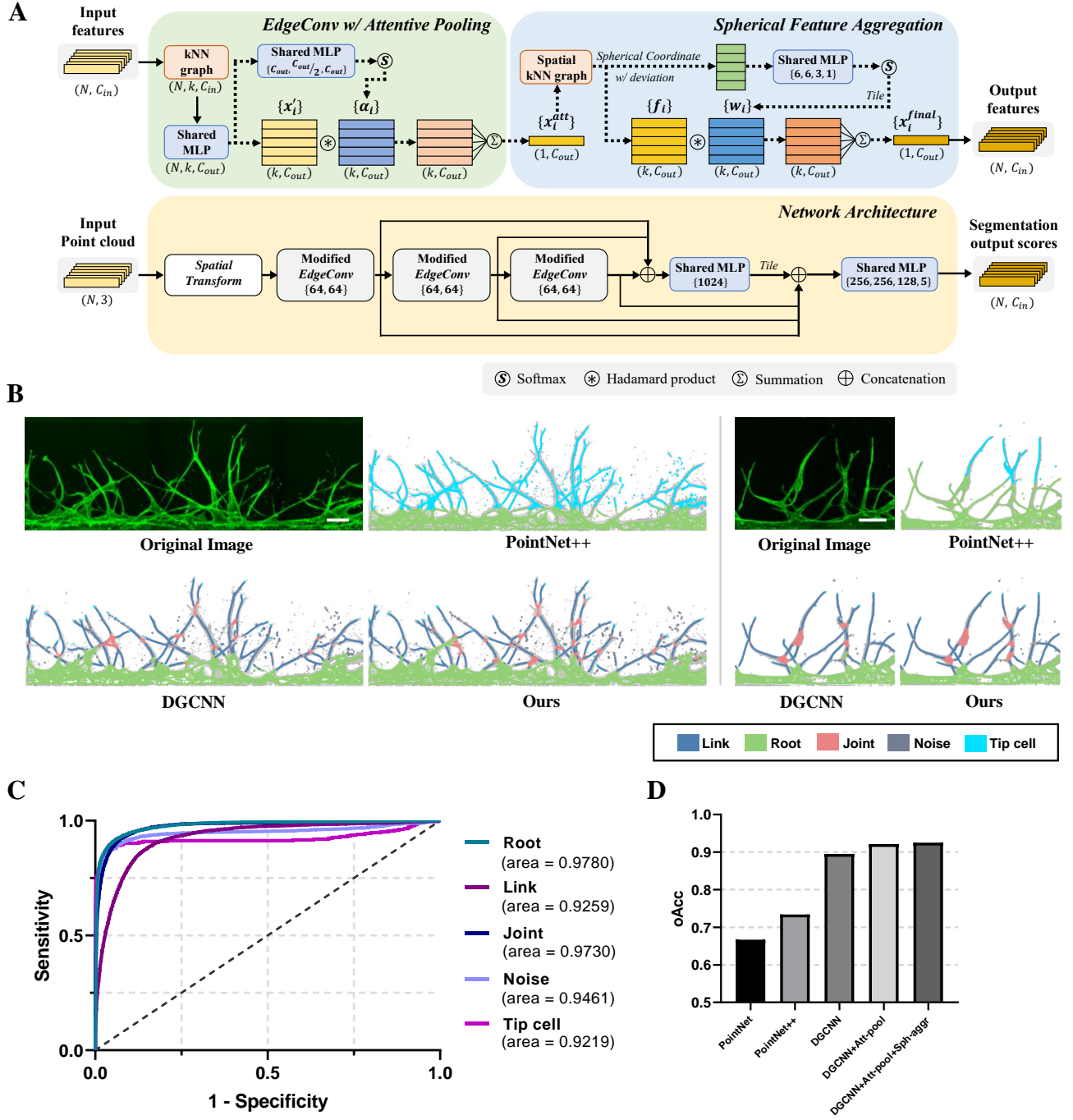
A

B

C

D

Fig. 4 Representation of the proposed network and comparison with other networks. (A) The overall architecture of our proposed mode used for skeleton segmentation. After EdgeConv, attention-pooling (green) and spherical feature aggregation (blue) modules are sequentially applied to weight the key neighboring features based on the local geometric context. Taking N points as input, per point segmentation scores are obtained after fusing global and local descriptors (yellow). Dropout layers with probability of 0.3 are used in the last MLPs. (B) Visual comparison of samples from angiogenesis dataset with different algorithms. Scale bars, 200 μm. (C) The receiver operating characteristic (ROC) curve of the proposed network for skeleton segmentation. (D) Comparison of accuracy with different algorithms, showing that the proposed network produced the highest overall accuracy among the algorithms tested after the same number of training epochs.

and function of the final skeleton from the initial raw contraction [15,36,37]. However, while the overall structure of on-chip angiogenesis may be complicated, the individual segments are simple enough that the initial raw contraction can faithfully mirror the original vascular structure. In this regard, the key concept

here is to leave the decision to GCN without adding any additional algorithms or contractions to confirm the branch and other functionalities of the initial raw contraction form. The approach developed by *Wu et al.* [17] for meso-skeleton extraction was chosen primarily because of its additional optimization methods that help
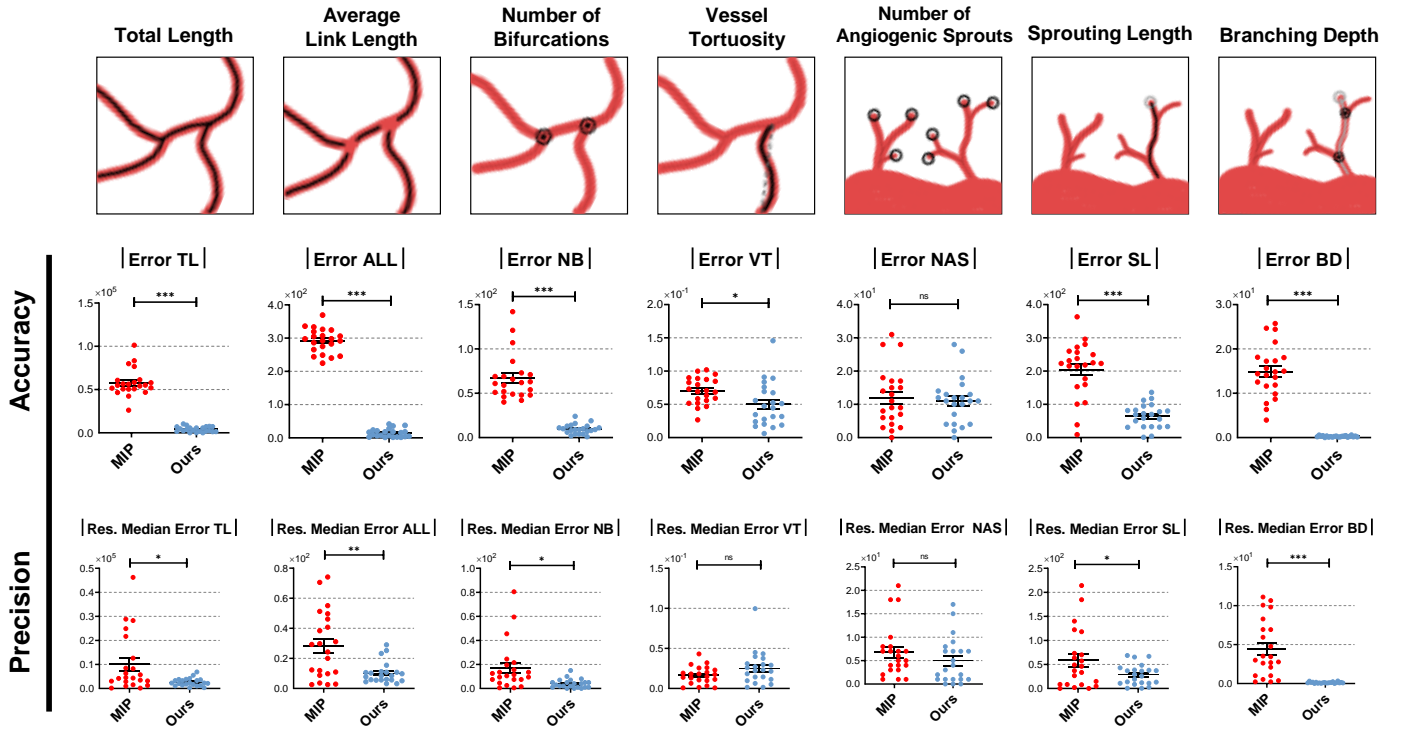
Fig. 5 Comparison of resultant parameters for angiogenesis analysis. Absolute error and the absolute residual error to the group's median error for the following variables were assessed and compared to the MIP method: total length (μm), average link length (μm), number of bifurcations, vascular tortuosity, number of angiogenic sprouts, sprouting length (μm), and branching depth. Our method demonstrates higher accuracy and precision across evaluation metrics compared to the conventional MIP method. Bars indicate mean $\pm$SEM. *p $<$ 0.05, **p $<$ 0.005, and ***p $<$ 0.0005 in the paired two-tailed Student's t-tests (N = 22 samples).

in uniform distribution of skeletal points and better preservation of the original structure. Upon this method, link optimization is only conducted on points with a directionality degree larger than a predefined threshold, so that each link or branch of the vasculature can have its own contraction behavior: alignment or repulsion. As a result, the branch is represented as a local point cluster, the link as skeletal curves, the root part as a large, continuous skeletal sheet at the bottom, and the noise part as a random speckle. Such a function-specific point distribution enables GCN, as explained later, to segment the relevant skeleton based on the local context of each point.

3.3 Network Optimization

Each point in extracted skeleton exists in an unstructured fashion without explicit cues for part segmentation. The conventional algorithms determine certain specified points from the original raw contraction, or meso-skeleton, as branch points based on their own algorithm while the remaining points are confirmed as links by extra-shrinking for the final skeleton extraction [15,16,38]. However, we found that the meso-skeleton already faithfully reflects the underlying structure of the angiogenic network, allowing us to detect each skeleton point's functioning immediately without further contraction. To precisely assess the angiogenic structure, with the employment of a deep learning network, each skeleton point was segmented into five functionalities: root,

link, joint, noise, and tip-cell. The functioning of the skeleton which is to be predicted depends heavily on the local context of each point. Therefore, DGCNN, which directly utilizes information about neighborhood connectivity, was chosen as our baseline model. In fact, neither PointNet [39] nor PointNet++ [40], which conduct feature embedding solely on the coordinate values of each point, produce satisfactory results (Fig. 4B, Fig. S2†). On the other hand, DGCNN performed somewhat better, thereby indicating GCN's superior ability to capture skeleton data's geometric context.

While the vanilla DGCNN performs rather well in terms of overall segmentation, it falls short in terms of tip cell recognition. To address this issue, attention pooling was implemented, which increased the tip cell detection capabilities (Fig. S3B†). Meanwhile, the spherical feature aggregation module not only achieved spatial uniformity of predicted functionality, but also enhanced tip cell detection capabilities as well (Fig. S3A†). In proposed aggregation module, with contrast to low-level features, high-level features tend to aggregate in regard to a certain direction, i.e., the orientation of angiogenesis (Fig. S3C†). A typical tip cell skeleton point has link points in the root direction and noise or meaningless points in the top direction. In light of these structural traits, it can be seen that having biased attention to root direction increased tip cell detection sensitivity by acquiring more meaning information for tip cell identification.

In conclusion, it can be observed that our modules, which

achieved the highest overall accuracy when compared to other models, function synergetically with GCN to execute skeleton segmentation (Fig. 4D). The capacity of such a network aids in a more thorough structural analysis of the specific angiogenic network.

3.4 Pipeline Evaluation

Each skeleton's 2400 point patches were retrieved and subjected to segmentation network for evaluation. The original skeleton was then recomposed and final 3D graph was obtained by using a DBSCAN algorithm and a post-processing step. When the accuracy of overall evaluation metrics was examined, our method had lower mean absolute error than that of MIP method (68.3% reduction) (Fig. 5). In the case of number of angiogenic sprouts, it can be observed that the difference is not so significant because tip cells in a 3D angiogenic network are seldom covered by other regions since they reside at the end of the network. When the precision of overall assessment metrics was tested in the same way, our technique exhibited a lower mean random error (47.9% reduction) than the MIP method.

The proposed method was further evaluated with the Bland-Altman analysis (Fig. S4†). Taking ground truth as a gold standard, the new technique's acceptability and appropriateness can be inferred by the visual inspection of error distribution[41,42]. Even though in the absence of absolute criteria regarding what magnitude should the range of the agreement interval must be in for establishing consensus, the results are still able to yield some insight into how well these measurements work relative to each other[32]. As a result, it was established that our analytical strategy provided results that were superior than MIP for almost all assessment criteria and resulted in data that was almost bias-free.

MIP method's erroneous results mainly ascribe to two reasons. One is that bulk parts of the projection image would inevitably be thinned to generate redundant skeleton fragments, leading to a distorted representation of the MVNs. Especially, the root of angiogenesis and different filtering processes for denoising have exacerbated such errors and inaccuracies. The other is that image projection poses a huge obstruction to computational interrogation of individual components. For instance, overlayed links generated spurious nodes and shortened respective lengths of vessels. Considering the global trend toward the complication of the microfluidic platforms and reconstructed vessel networks, it is obvious that such blunders will potentially hinder getting the correct information in the future study. 3D assessment of MVNs can settle this issue to some degree. The previous voxel-based technique, for example, Imaris (Bitplane Scientific Software), has demonstrated considerable success in this respect, but its performance in the field of on-chip MVN analysis remains disappointing. Their data representation is computationally heavy and fragile to background noises. Besides, morphological closing to fill gaps in regions of capillaries must be preceded for skeleton extraction, which requires laborious human intervention or prior knowledge of vascular diameter[10,43].

By doing much of the analysis directly in the 3D point cloud domain, our work-around bypasses many of these difficulties. Ex-

perimental results indicate the suggested method's promising capability to extract features directly in the 3D point clouds with substantial accuracy even comparable to manual measurement. Its geometrically accurate representation of individual functional parts would be of great value in quantifying phenotypic variation and further diversifying oversimplified current approaches for on-chip MVN evaluation. To our best knowledge, this is the first work to apply the deep learning framework to analyze 3D MVNs in an organ-on-a-chip platform. In this respect, we anticipate that the present work might offer some fresh perspectives on vessel image processing issues, and potentially also several advantages over existing techniques.

4 Conclusions

In this paper, we have developed a machine learning-assisted method for the evaluation and quantification of angiogenesis' morphological features on the MV-IMPACT platform. The key idea is to summarize MVN into meso-skeleton which enables an accurate depiction of the original architecture, and then segment the skeleton into different functional components using GCN. With the guidance of designed modules, our network could effectively capture geometrical context and finely delineate the border of individual parts. Experiment results indicate that our proposed method outperforms the conventional MIP method in all seven assessment criteria, making it more accurate and precise in quantifying phenotypic variation. Our methodology, tailored for *on-chip* microvasculature, provides a robust framework for logically analyzing 3D angiogenesis datasets. We believe that the principles developed within this work can be applied to many other organ-on-a-chip platforms with varying design shapes and biochemical milieu.

Data Availability

The codes used for skeleton segmentation and network evaluation are available here.

Author Contributions

WL conceived the overall concept and design of this work. WL conducted the experiment, designed the machine learning algorithm, analyzed the data, and wrote the manuscript. BY analyzed the data, contributed to data annotation and quantitative analysis, and designed the figures. JL and SJ performed technical and experimental supports. NLJ supervised all work. All the authors read and approved the final manuscript.

Conflicts of interest

The authors have no conflicts of interest to declare

Acknowledgements

Not applicable.

Notes and references

1 D. Hanahan and R. A. Weinberg, *cell*, 2000, **100**, 57–70.
2 M. W. Laschke, Y. Harder, M. Amon, I. Martin, J. Farhadi, A. Ring, N. Torio-Padron, R. Schramm, M. Rücker, D. Junker *et al.*, *Tissue engineering*, 2006, **12**, 2093–2104.

3 K. Schmidt-Bleek, B. J. Kwee, D. J. Mooney and G. N. Duda, *Tissue Engineering Part B: Reviews*, 2015, **21**, 354–364.

4 S. N. Bhatia and D. E. Ingber, *Nature biotechnology*, 2014, **32**, 760–772.

5 S. Kim, H. Lee, M. Chung and N. L. Jeon, *Lab on a Chip*, 2013, **13**, 1489–1500.

6 M. Chung, J. Ahn, K. Son, S. Kim and N. L. Jeon, *Advanced healthcare materials*, 2017, **6**, 1700196.

7 N. Jährling, K. Becker and H.-U. Dodt, *Organogenesis*, 2009, **5**, 227–230.

8 S. Bash, J. P. Villablanca, R. Jahan, G. Duckwiler, M. Tillis, C. Kidwell, J. Saver and J. Sayre, *American journal of neuroradiology*, 2005, **26**, 1012–1021.

9 I. D. Kelch, G. Bogle, G. B. Sands, A. R. Phillips, I. J. LeGrice and P. Rod Dunbar, *Scientific reports*, 2015, **5**, 1–19.

10 P. Gkontra, K.-A. Norton, M. M. Żak, C. Clemente, J. Agüero, B. Ibáñez, A. Santos, A. S. Popel and A. G. Arroyo, *Scientific reports*, 2018, **8**, 1–19.

11 K. W. Eliceiri, M. R. Berthold, I. G. Goldberg, L. Ibáñez, B. S. Manjunath, M. E. Martone, R. F. Murphy, H. Peng, A. L. Plant, B. Roysam *et al.*, *Nature methods*, 2012, **9**, 697–710.

12 E. Zudaire, L. Gambardella, C. Kurcz and S. Vermeren, *PloS one*, 2011, **6**, e27385.

13 T.-C. Lee, R. L. Kashyap and C.-N. Chu, *CVGIP: Graphical Models and Image Processing*, 1994, **56**, 462–478.

14 P. Kollmannsberger, M. Kerschnitzki, F. Repp, W. Wagermaier, R. Weinkamer and P. Fratzl, *New Journal of Physics*, 2017, **19**, 073019.

15 H. Huang, S. Wu, D. Cohen-Or, M. Gong, H. Zhang, G. Li and B. Chen, *ACM Trans. Graph.*, 2013, **32**, 65–1.

16 J. Zhou, J. Liu and M. Zhang, *International Journal of Applied Mathematics and Computer Science*, 2020, **30**, 123–132.

17 S. Wu, H. Huang, M. Gong, M. Zwicker and D. Cohen-Or, *ACM Transactions on Graphics (ToG)*, 2015, **34**, 1–13.

18 S. Kim, M. Chung, J. Ahn, S. Lee and N. L. Jeon, *Lab on a Chip*, 2016, **16**, 4189–4199.

19 Y. Wang, Y. Sun, Z. Liu, S. E. Sarma, M. M. Bronstein and J. M. Solomon, *Acm Transactions On Graphics (tog)*, 2019, **38**, 1–12.

20 S. Ioffe and C. Szegedy, International conference on machine learning, 2015, pp. 448–456.

21 A. L. Maas, A. Y. Hannun and A. Y. Ng, Proc. icml, 2013, p. 3.

22 S. Qiu, S. Anwar and N. Barnes, Proceedings of the IEEE/CVF Winter Conference on Applications of Computer Vision, 2021, pp. 3813–3822.

23 J. Hu, L. Shen and G. Sun, Proceedings of the IEEE conference on computer vision and pattern recognition, 2018, pp. 7132–7141.

24 Y. Yang, Y. Ma, J. Zhang, X. Gao and M. Xu, *Sensors*, 2020, **20**, 5455.

25 M. Ester, H.-P. Kriegel, J. Sander, X. Xu *et al.*, kdd, 1996, pp. 226–231.

26 A. D. van der Meer, V. V. Orlova, P. ten Dijke, A. van den Berg and C. L. Mummery, *Lab on a Chip*, 2013, **13**, 3562–3568.

27 J. A. Whisler, M. B. Chen and R. D. Kamm, *Tissue engineering part C: methods*, 2014, **20**, 543–552.

28 V. Van Duinen, D. Zhu, C. Ramakers, A. Van Zonneveld, P. Vulto and T. Hankemeier, *Angiogenesis*, 2019, **22**, 157–165.

29 S. Kim, J. Ko, S.-R. Lee, D. Park, S. Park and N. L. Jeon, *Biotechnology and Bioengineering*, 2021, **118**, 2524–2535.

30 J. Yu, S. Lee, J. Song, S.-R. Lee, S. Kim, H. Choi, H. Kang, Y. Hwang, Y.-K. Hong and N. L. Jeon, *Nano Convergence*, 2022, **9**, 1–11.

31 M. B. Brown and A. B. Forsythe, *Journal of the American statistical association*, 1974, **69**, 364–367.

32 B. A. Corliss, R. W. Doty, C. Mathews, P. A. Yates, T. Zhang and S. M. Peirce, *Microcirculation*, 2020, **27**, e12618.

33 Z. Chen, N. Ma, X. Sun, Q. Li, Y. Zeng, F. Chen, S. Sun, J. Xu, J. Zhang, H. Ye *et al.*, *Biomaterials*, 2021, **272**, 120770.

34 L. Abdul, S. Rajasekar, D. S. Lin, S. V. Raja, A. Sotra, Y. Feng, A. Liu and B. Zhang, *Lab on a Chip*, 2020, **20**, 4623–4631.

35 D. Lesage, E. D. Angelini, I. Bloch and G. Funka-Lea, *Medical image analysis*, 2009, **13**, 819–845.

36 J. Cao, A. Tagliasacchi, M. Olson, H. Zhang and Z. Su, 2010 Shape Modeling International Conference, 2010, pp. 187–197.

37 V. Jayadevan, E. Delp and Z. Pizlo, *arXiv preprint arXiv:1912.11932*, 2019.

38 A. Tagliasacchi, H. Zhang and D. Cohen-Or, *ACM SIGGRAPH 2009 papers*, Association for Computing Machinery, 2009, pp. 1–9.

39 C. R. Qi, H. Su, K. Mo and L. J. Guibas, Proceedings of the IEEE conference on computer vision and pattern recognition, 2017, pp. 652–660.

40 C. R. Qi, L. Yi, H. Su and L. J. Guibas, *Advances in neural information processing systems*, 2017, **30**, year.

41 D. G. Altman and J. M. Bland, *Journal of the Royal Statistical Society: Series D (The Statistician)*, 1983, **32**, 307–317.

42 J. M. Bland and D. Altman, *The lancet*, 1986, **327**, 307–310.

43 S. K. Stamatelos, E. Kim, A. P. Pathak and A. S. Popel, *Microvascular research*, 2014, **91**, 8–21.